

Pyroclastic flow erosion and bulking processes: comparing field-based vs. modeling results at Tungurahua volcano, Ecuador

Julien Bernard · Karim Kelfoun · Jean-Luc Le Pennec ·
Silvia Vallejo Vargas

Received: 19 November 2013 / Accepted: 3 August 2014 / Published online: 13 August 2014
© Springer-Verlag Berlin Heidelberg 2014

Abstract Pyroclastic density currents (PDCs) are high-temperature and high-velocity mixtures that threaten populations in the vicinity of many active volcanoes. Deciphering the cause of their remarkable mobility is essential for volcanic hazard analysis, but remains difficult because of the complex processes occurring within the flows. Here, we investigate the effect of bulking on dense PDC mobility by means of a double approach. First, we estimate the amount of material incorporated into scoria flows emplaced during the August 2006 eruption of Tungurahua volcano, Ecuador. For this, we carry out a detailed analysis of 3D-corrected digital images of well-exposed scoria flow deposits. Componentry analysis indicates that PDC bulking occurs principally on the steep ($>25^\circ$) upper slope of the volcano, and the deposits typically comprise 40–50 wt% of non-juvenile (i.e., accessory and accidental) material. Secondly, we develop a simple stress-related grain-by-grain equation of erosion combined with two simple depth-averaged geophysical mass-flow models that compare the bulking mechanism to a non-fluidized and a fluidized flow. Two behaviors based on Coulomb and plastic rheologies are

used to reproduce, on a first order basis, the 2006 Tungurahua PDCs. Cross-check comparisons between these modeled cases and the erosion pattern inferred from field-based data allow us to evaluate the accuracy of our modeling assumptions. Regardless of the rheological regime, the PDC-induced erosion pattern of the 2006 Tungurahua eruption can only be reproduced by fluctuations of the flow's basal shear stress during emplacement. Such variations are controlled by flow thinning-thickening processes, notably through the formation of a thick non-erosive flow body that pushes a thin frictional erosive front during PDC emplacement. The input volume of juvenile material, as well as the thickness of the erodible layer available prior to the eruption, are additional key parameters. Our work highlights complexities in PDC erosion and bulking processes that deserve further study. In terms of hazard assessment, our findings reveal that incorporation and bulking translate into increased flow mobility, i.e., the augmented flow mass enhances both flow velocity and runout distance (up to 20 %). These outcomes should be considered closely for hazard analysis at many other andesitic volcanoes worldwide where similar PDC events are common.

Editorial responsibility: V. Manville

Electronic supplementary material The online version of this article (doi:10.1007/s00445-014-0858-y) contains supplementary material, which is available to authorized users.

J. Bernard (✉) · K. Kelfoun · J.-L. Le Pennec
Clermont Université, Université Blaise Pascal, Laboratoire Magmas
et Volcans, BP 10448, 63000 Clermont-Ferrand, France
e-mail: j.bernard@opgc.univ-bpclermont.fr

J. Bernard · K. Kelfoun · J.-L. Le Pennec
CNRS, UMR 6524, LMV, 63038 Clermont-Ferrand, France

J. Bernard · K. Kelfoun · J.-L. Le Pennec
IRD, R 163, LMV, 63038 Clermont-Ferrand, France

S. Vallejo Vargas
Instituto Geofísico, Escuela Politécnica Nacional, Quito, Ecuador

Keywords Pyroclastic density currents · Erosion ·
Componentry · Numerical simulation · Tungurahua

Introduction

Pyroclastic density currents (PDCs) are highly mobile mixtures of blocks, lapilli, ash, and hot volcanic gas produced during explosive eruptions. Their flow behavior defines a continuum between dilute, turbulent and dense, granular end-members. Most dense PDCs are high-velocity flows with potentially long runout distances and represent the most deadly phenomena associated with volcanic activity, with tens of thousands of lives claimed in the past millennium

(Tanguy et al. 1998; Auker et al. 2013). Understanding the origin of the remarkable mobility and velocity of PDCs is therefore a major research issue in volcanology that has stimulated numerous studies using field, analogue, and numerical approaches (e.g., Sparks 1976; Sparks et al. 1978; Druitt 1998; Branney and Kokelaar 2002; Dellino et al. 2010; Kelfoun 2011; Jessop et al. 2012; Roche et al. 2013 and references therein).

Many previous studies have documented the complex componentry assemblage of natural PDC deposits (e.g., Buesch 1992; Boudon et al. 1993; Sparks et al. 1997; Calder et al. 2000; Gurioli et al. 2002; Saucedo et al. 2004; Cole et al. 2005; Lube et al. 2007; Charbonnier and Gertisser 2011; Brand et al. 2014), which all show evidence of incorporation of accessory and accidental material (in the sense of Cas and Wright 1987; hereafter referred to as “non-juvenile” material) during emplacement.

Observations of debris flows, avalanches, or landslides coupled with laboratory experiments have been used in previous studies to formulate theoretical equations of substrate entrainment. Earlier experimental and numerical attempts at reproducing erosion at the base of granular flows have shown that slope angle, flow velocity, thickness and internal particle concentration, shear stress and mass transfer processes near the flow base, pore-pressure and plowing effects are, among other parameters, essential in controlling the erosion type and rate triggered by granular flows and snow avalanches (Egashira et al. 2001; Fraccarollo and Capart 2002; Naaim et al. 2003; Pitman et al. 2003; Cao et al. 2004; Mc Dougall and Hungr 2005; Sovilla et al. 2006; Mangeney et al. 2007, 2010; Bouchut et al. 2008; Medina et al. 2008; Iverson et al. 2011; Mc Coy et al. 2012; Iverson 2012; Pirulli and Pastor 2012; Quan Luna et al. 2012; Roche et al. 2013; Farin et al. 2013 and references therein). Importantly, laboratory experiments reveal that the erosion processes associated with the emplacement of dry granular flows increase their velocity and runout distance (up to 40–50 %) when the slope angle is set close to the friction angle of the bed material (Mangeney et al. 2010; Farin et al. 2013). Overall, previous field studies and these analogue models of clast incorporation into granular flows point to complex entrainment mechanisms. Concomitantly, detailed theoretical and numerical investigations have led to the definition of various equations for the erosion rate E , which predict that volume and mass growth of wet and dry granular flows through erosion and incorporation are described either by an exponential law (Mc Dougall and Hungr 2005; Crosta et al. 2009; Pirulli and Pastor 2012), or by a monotonic increase in the amount of eroded material with the basal shear stress when a given threshold is exceeded (Pitman et al. 2003). Such theoretical formulations rely on the assumptions that E is essentially controlled by the rheological behavior of the flow and the mechanical properties of the erodible bed. These studies mostly focus on debris flows,

landslides, and rock or snow avalanches, so the influence of bed erosion and material incorporation on PDC mobility and velocity has not been fully clear in previous numerical works (Lê and Pitman 2009).

In this paper, we consider the influence of erosion processes on PDC behavior by means of a double approach. Firstly, we estimate the amount of erosion incorporation of non-juvenile material in natural dense granular PDC deposits using data from well-exposed scoria-flow deposits of the August 2006 Tungurahua volcano eruption in Ecuador. The componentry study is based on the analysis of high-resolution images of selected exposures in the field. Secondly, we focus on the influence of basal shear stresses commonly used in numerical simulations of PDCs (i.e., Coulomb and plastic rheologies) to compare the 2006 erosion pattern inferred from the above image analysis data with that reproduced by the modeling approach. We define a simple erosion law based on the balance of external forces exerted on a particle from the erodible bed and submitted to PDC shearing. This erosion law is incorporated into the VolcFlow depth-averaged numerical code (Kelfoun and Druitt 2005), which allows different rheological flow behaviors to be tested on DEM-derived slopes. In addition, as shown in a previous work, our approach has potential for hazard assessment purposes (Pitman et al. 2003; Kelfoun et al. 2009; Charbonnier and Gertisser 2012).

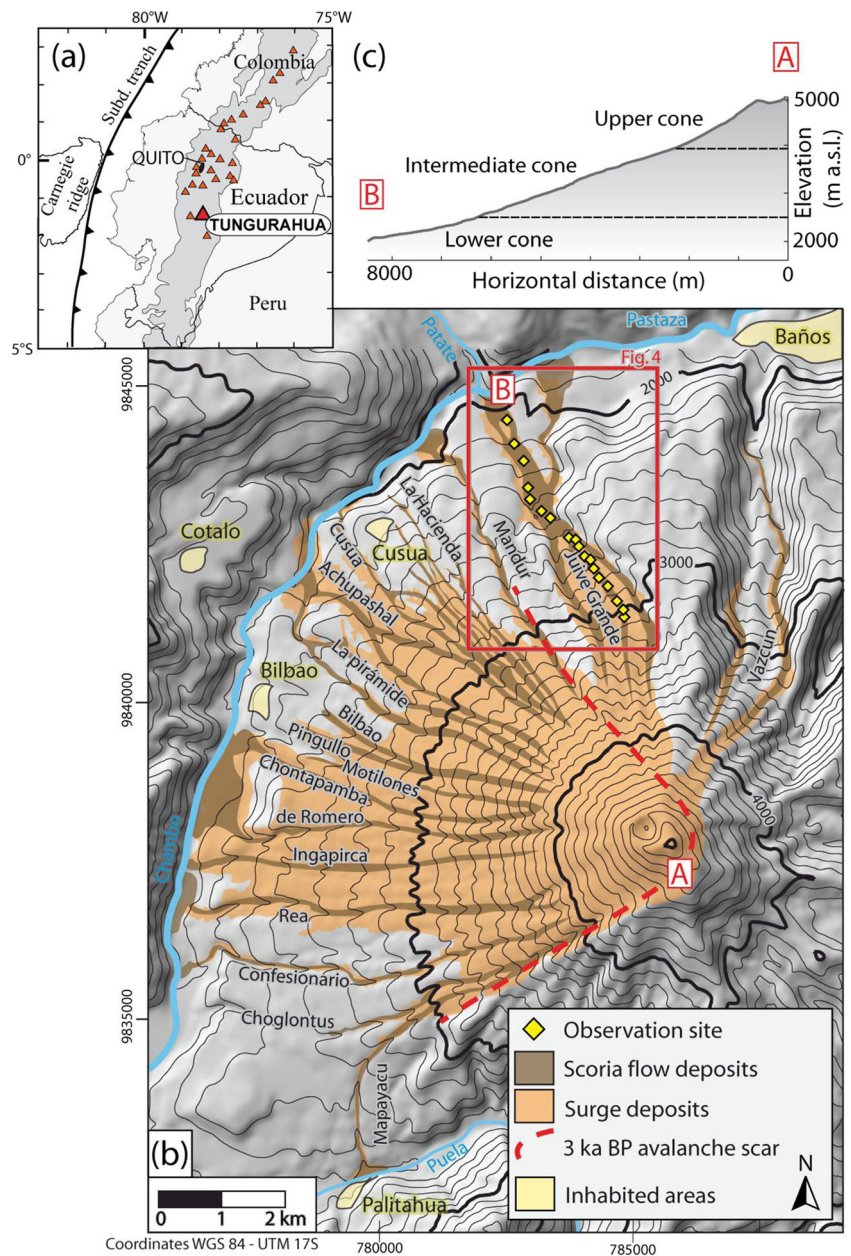
In this study, we call the non-erodible part of the PDC channel bedrock the “substrate” and the superficial potentially removable layer the “erodible bed.” Following Iverson (2012), “entrainment” is the incorporation process of solid particles that does not change bulk flow composition, and “bulking” is defined as a clast-incorporation process that increases the flow’s volumetric solid fraction. The expression “erosion pattern” is used to describe the main characteristics of the PDC-induced entrainment and incorporation processes and effects (i.e., erosion intensity and localization along PDC paths).

Geological settings

Tungurahua volcano and the 2006 eruption

Tungurahua (5,023 m asl) is a steep-sided andesitic stratocone located in the Eastern Andean Cordillera of Ecuador (Fig. 1a, b). Recent geological investigations show that PDC-forming eruptions have occurred in the past millennium at a rate of at least one per century (Hall et al. 1999; Le Pennec et al. 2008, 2013). About 25,000 inhabitants living on the northern, western, and southern sides of the edifice are potentially threatened by the volcano. After 80 years of repose, a new eruptive period started in 1999, with subsistent explosive activity of uneven intensity and style (e.g., periods of

Fig. 1 **a** Location map of Tungurahua volcano in Ecuador. In gray, Andean relief above 2,000 m asl; triangles volcanoes active during the past 10,000 years. **b** Map of Tungurahua 2006 pyroclastic flow deposits (PDC deposits in dark brown and surge deposits in orange) plotted on a shaded DEM of the edifice (modified from Kelfoun et al. 2009). Red rectangle corresponds to the extent of Fig. 4. **c** Section along profile A–B showing the three morphological domains described in the text



complete quiescence and sporadic stronger strombolian to subplinian events, Carn et al. 2008; Le Pennec et al. 2012; Eychenne et al. 2013). The erupted magma has a homogeneous andesitic composition (58–59 wt% SiO₂), with minor subdacitic pumice in August 2006 (61–63 wt% SiO₂; Samaniego et al. 2011).

The strong and deadly 16th–17th August 2006 PDC-forming eruption had a rank of VEI 4 based on satellite remote sensing data (Fee et al. 2010) while tephra studies and monitoring data point to a VEI 3 subplinian event (Eychenne et al. 2012, 2013; Hall et al. 2013). This event has been thoroughly documented in recent studies (Arellano et al. 2008; Kelfoun et al. 2009; Steffke et al. 2010; Eychenne et al. 2012, 2013;

Hall et al. 2013; Douillet et al. 2013) and is used below as a test case to investigate entrainment-incorporation processes in dense PDCs.

Cone structure and 2006 PDC deposits architecture

The Tungurahua edifice has a broad conical shape with a rugged, eroded eastern part and a fairly smooth and regular western part (Fig. 1; Hall et al. 1999). We divide the E–W profile of the young Tungurahua edifice into three main morphological domains. The domain near the summit, above ~3,500 m asl, is referred to here as the “upper cone” and is characterized by steep slopes (35–45°) with a rough drainage

network. The “intermediate cone” lies between 3,500 and 2,300 m asl, about 2.5–6 km from the vent, where the slope gradually decreases from 30–35 to 20° and the morphology is rugged with pronounced gullies. The base of the volcano below 2,300 m asl has a smooth landscape with gentle slopes (10–20°) cut by a few ravines and is referred to here as the “lower cone.”

Large-scale features of the 2006 PDCs and surges are described in Hall et al. (2013) and Douillet et al. (2013). Here, we focus on the Juive Grande area, located on the northwestern side of the volcano (Fig. 1), which was affected by many PDC phases of the 2006 eruption (Hall et al. 2013). By the time of our field work, in March 2012 and October 2013, most 2006 PDC deposits had been incised down to the base by narrow gullies, exposing spectacular subvertical sections.

2006 PDC deposits in the Juive Grande area

In the Juive Grande area, the PDC deposits display significantly different features in the three morphological domains described above. Observations and thermal infrared images captured during the eruption indicate that no pyroclastic flow deposits were emplaced above 3,800 m asl, on slope angles >25–30° (Kelfoun et al. 2009). From this observation and our field surveys, we infer that PDC sedimentation most likely began as patchy deposits between 3,800 and 3,300 m asl. On the intermediate cone of Juive Grande (3,300 to 2,200 m asl), the 2006 PDCs were channelized in the gullies. The deposits can be traced as a continuous ravine-ponded breccia with a subflat-topped surface morphology formed by the stacking of discrete flow units. The overall thickness at ~3,300 m asl is in the order of 1–2 m and increases downslope to 3–5 m at 2,300 m asl. In the Juive lower cone area (2,300–1,900 m), the morphology is smoother and the flows generally unconfined. Pyroclastic fans (50–150 m wide) were formed in the Pastaza river valley (Fig. 1) by the overlapping of PDC flow units. Each flow unit is typically 1–2 m thick at the front, with a channel width of 3–7 m where well-developed levees are preserved in each flow tongue higher on the slopes. In vertical sections, the deposits show common reverse coarse-tail grading and cauliflower bombs at the top. Quarries in the 2006 deposits at Juive Grande (Fig. 1) expose a maximum thickness of 5–7 m of scoriaceous flow material.

In summary, the overall structure of the 2006 deposits is broadly correlated with the slope of the cone and the total thickness tends to increase downslope. No deposition occurred on the steepest slopes of the volcano (the upper cone, above ~3,500 m asl), and depositional processes began high on the intermediate cone. Similar depositional patterns have been documented at other andesitic volcanoes worldwide (e.g., Colima in Mexico, Saucedo et al. 2002; Sarocchi et al. 2011; Arenal in Costa Rica, Cole et al. 2005; Ngauruhoe in New Zealand, Lube et al. 2007; Merapi in Indonesia,

Charbonnier and Gertisser 2011), and are an essential feature for modeling purposes.

Methods

Our field work was carried out along a subradial, 4-km long transect in the Juive Grande valley, where the 2006 deposits are incised by ~5–10-m-deep ravines. Thickness, surface morphology, stratigraphy, grain size, grading, and componentry features of the scoriaceous PDC deposits were documented at 23 sites (Fig. 1). We selected eight sites to perform a detailed grain-size and componentry analysis of the deposits using a novel approach based on image analysis coupled with stereological conversion (based on image segmentation and stereological unfolding techniques). High-resolution images of selected deposits' sections were taken at several magnifications to capture grain componentry and shape for a large size range (~50 to ~0.2 cm; Fig. 2). Our workflow is illustrated in Fig. 3 and summarized in the [Supplementary electronic material \(SEM\)](#). A detailed description of the analytical protocol and results is beyond the scope of this paper and will be presented in a forthcoming contribution. The main steps are (1) image segmentation into discrete objects, representing each visible clast of the deposit sampled; (2) 2D componentry identification (i.e., juvenile or not), size, and shape measurement (circle equivalent area and diameter); (3) 2D to 3D stereological conversion (Sahagian and Proussevitch 1998; Shea et al. 2010) to obtain volume fraction of each clast family depending on its size, in ϕ -scale [$\phi = -\log_2$ (diameter in mm)]; and (4) volume-to-mass conversion using specific densities of each clast type. Areas where fragments are too small to be identified on the screen are referred to here as “digital background.” A sample, or “digital sample,” is thus defined here as the whole set of high-resolution digital images taken at different magnifications of a single pyroclastic flow unit at a given outcrop. Using a large set of images and different magnifications yields object populations in the range of 1,000–3,400 clasts per sample and gives 2D to 3D conversion errors of <5 % (Sahagian and Proussevitch 1998).

Tungurahua's scoria flow deposits are composed of easily distinguishable clast families and offer an exceptional opportunity to perform precise componentry analysis on medium and coarse size ranges (i.e., >1–2 ϕ). Juvenile andesitic clasts occur as scoriaceous cauliflower bombs and as dark-grey dense angular clasts. The non-juvenile class comprises four merged subclasses: subangular accessory lava, reddish oxidized fragments, accessory pumices, and rare accidental greenish gneissic clasts. Mass proportions of the whole sample are computed and take into account the fine fraction of the deposit [“matrix”, see [Supplementary electronic material \(SEM\)](#)]. Finally, our data are corrected using conduit-derived non-juvenile fragments [see [Supplementary electronic material](#)

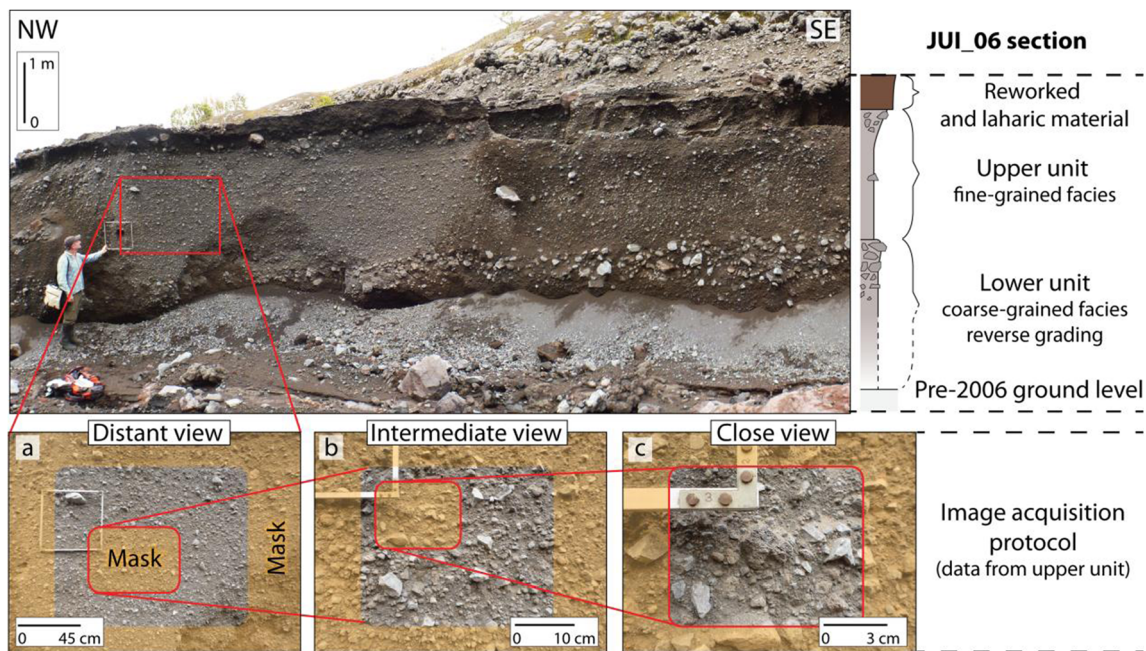


Fig. 2 Typical outcrop of the 2006 PDCs deposit of Tungurahua volcano with a stratigraphic log of the pyroclastic sequence. The image acquisition strategy used in this study is illustrated by images a–c, taken at different

magnifications. Exclusion masks (used to avoid double counting of clasts and to discard any optical or geometrical deformation at the edges of the images) are also illustrated in orange

(SEM)] to isolate only the non-juvenile mass fraction of the 2006 PDC deposits, which derives from the eroded substratum.

Componentry results: erosion pattern of 2006 PDCs

The smallest recognized ϕ classes of the samples occur between -1 and -1.5ϕ (2–2.8 mm). The mass proportion of the digital background (the unsegmented parts of the images,

see “Methods”) is between 23 and 74 wt%, with a mean of 47 ± 13 wt% (one standard deviation), which implies that the composition of about half of the mass of the deposits can be estimated using our “digital sampling” method.

Figure 4 presents the mass proportion of juvenile (gray) and non-juvenile (white) material for each whole sample of the Juive Grande valley. Each pie chart represents a sample, and “n” is the number of identified clasts used for the mass reconstruction. The mass proportion of non-juvenile material in the eight samples

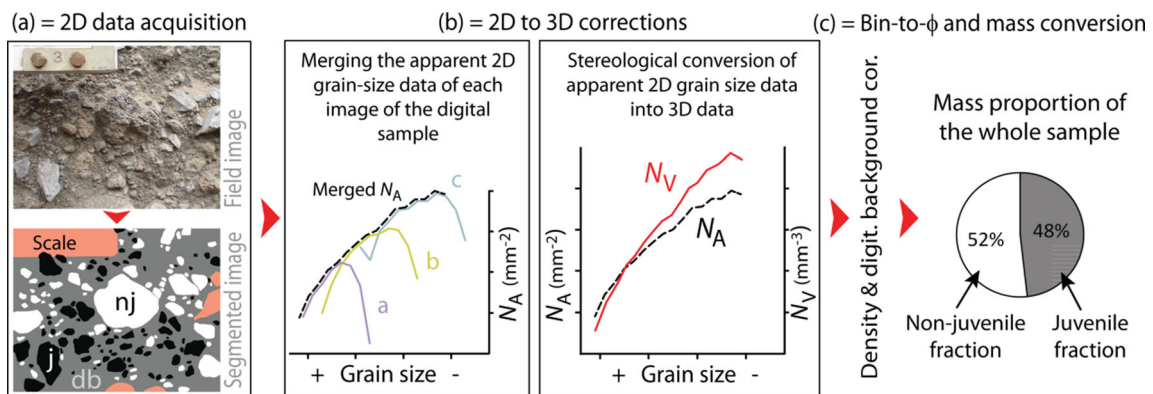
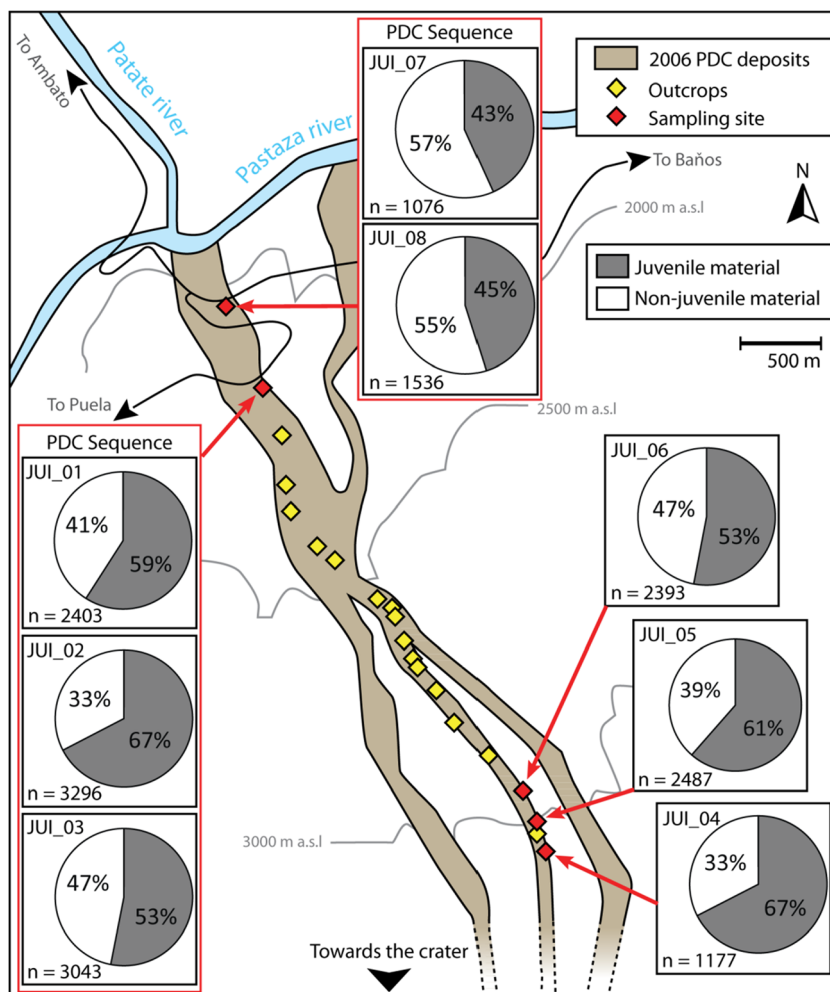


Fig. 3 2D to 3D workflow used in this study, see also [Supplementary electronic material \(SEM\) 1](#). **a** 2D data acquisition step: high resolution images filtering and segmentation into juvenile and non-juvenile fragments. On the segmented image, *db* (dark gray) is for “digital background”, *j* (black) for juvenile, and *nj* (white) for non-juvenile fragments. Red areas represent the exclusion mask (see Fig. 2). Segmented images are analyzed with SPO software (Launeau and Robin 1996). **b** The number density of clasts of a given size per unit area (N_A) of the whole digital sample is obtained using the merging cutoff technique of Shea

et al. (2010). **a–c** refer to different image magnifications of Fig. 2. N_A value is converted to clast number density of a given size per unit volume (N_V) using the stereological suite of Sahagian and Proussevitch (1998) detailed in Shea et al. (2010). Grain-size data are converted to phi scale (see text). **c** N_V is converted to masses, using measured specific densities of each clast type (juvenile and non-juvenile components, Eychenne and Le Pennec 2012). The total mass proportion of the sample is obtained by summing all mass fractions corresponding to each N_V , taking into account digital background proportions (see text)

Fig. 4 Mass proportions (%) of juvenile (in *gray*) vs. non-juvenile (in *white*) material of PDC deposits from eight samples of the Juive Grande area (see Fig. 1 for location). “JUI” denotes sample numbers. “n” is the number of identified clasts in each sample. JUI_07, JUI_08, and JUI_01, JUI_02, JUI_03 belong to different flow units of the same site in stratigraphic order



ranges from 57 to 33 wt% (JUI_07 and JUI_04 samples, respectively). Deposits emplaced at $\sim 3,300$ m asl comprise ~ 40 wt% of non-juvenile material (Fig. 4), which indicates that the erosion processes mainly occurred at a higher elevation. The mass proportion of substrate-derived material is remarkably constant in all samples (around 40–50 wt%, Fig. 4), which implies that the amount of erosion is low along the studied transect. Thus, erosion and incorporation occur in the upper cone domain and high in the intermediate cone domain (slopes $> 25^\circ$) and are low on slopes of $< 25^\circ$. These main features characterize the “erosion pattern” of the 2006 PDCs in the Juive Grande area and are used below to evaluate the accuracy of our numerical models.

Modeling

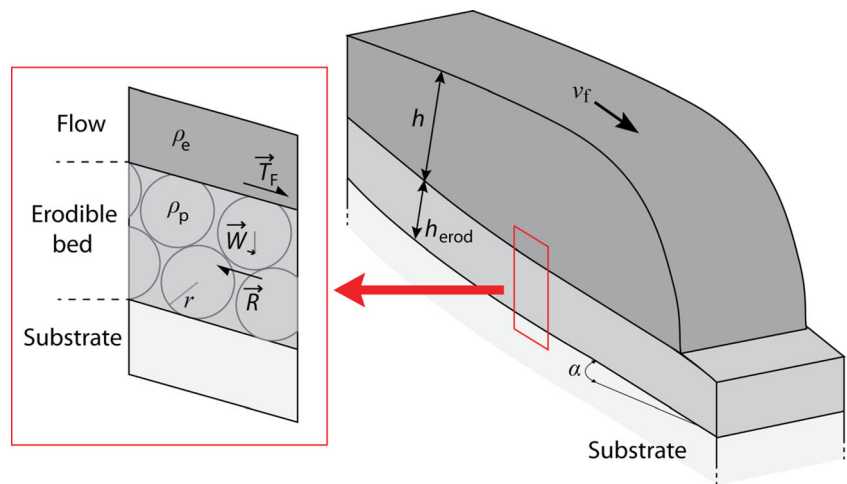
Shear stress-related erosion

We consider here the schematic case of an erodible granular layer comprising an assemblage of spherical particles of

radius r and bulk density ρ_p lying above a static substratum (Fig. 5 and Table 1). If not influenced by a PDC, the erodible layer stability is a function of the equilibrium between (1) the weight of the particles, whose downstream component W depends on the slope α of the flank, and (2) the retarding forces R related to the normal component of the particle weight, to the friction angle φ and to the cohesion C of the erodible bed. A descending PDC disturbs the erodible bed in two opposite ways: (a) the basal shear force $T_F = T \times S_f$ (where T is the basal shear stress and S_f the contact surface between the flow and the particle) of the flow tends to entrain the erodible particles downstream; (b) at the same time, the flow weight increases the normal stress at the base of the erodible particle, thus increasing R and stabilizing the erodible layer. The erosive potential of the PDC and the associated bulking effect depends on the equilibrium between these two effects.

We state that a particle is entrained and incorporated into the flow when it has moved a distance greater than its own diameter. Newton’s second law states that the sum of external

Fig. 5 Schematic view of the system modeled in this study. A PDC of thickness h and density ρ_e is moving down a slope of angle α with a velocity V and covers an erodible bed of thickness h_{erod} composed by spherical particles of radius r and density ρ_p above a non-erodible substrate. \vec{T}_F is the flow basal shear force acting at the top of the particles, \vec{W} the downstream component of particle weight, and \vec{R} is the retarding force at the base of the particle (see also Table 1)



forces F (written in this paper under their norm, $\|\vec{F}\| = F$) acting on a body is proportional to the product of its acceleration term dv/dt (where v is velocity and t is time) and its mass m , as:

$$F = m \frac{dv}{dt} \tag{1}$$

where the net forces F acting upon a particle of the erodible bed disturbed by a flow are $F=W+T_F-R$. Integration of the acceleration term yields the velocity v_p of the removed particle, which is expressed at a given time t_1 by:

$$v_p = \int_{t=0}^{t=t_1} \frac{F}{m} \times dt = \frac{F}{m} \times t_1 \tag{2}$$

because F does not depend on the flow velocity whatever the rheological behavior is (see “Rheology and nature of PDCs”). The distance D travelled by a particle entrained in the PDC during the same time t_1 is obtained by the integration of the velocity:

$$D = \int_{t=0}^{t=t_1} \frac{F}{m} \times t_1 \times dt = \frac{1}{2} \frac{F}{m} \times t_1^2 \tag{3}$$

However, a particle is accelerated only when its velocity is lower than that of the flow, and both reach equal velocities after a given duration. The time t_{er} required to entirely incorporate a particle of diameter $2r$ from the erodible bed during the acceleration phase is given by inverting Eq. (3) as:

$$t_{er} = 2 \sqrt{\frac{r m}{F}} \tag{4}$$

A particle that is not totally removed during the acceleration phase reaches the flow velocity before completely leaving

its position. We determine t_v , the time needed to accelerate a particle to the flow velocity v_f , by inverting Eq. (2) with $v_p=v_f$:

$$t_v = \frac{m}{F} v_f \tag{5}$$

The distance D_v travelled by the particle during the acceleration time t_v is given by Eq. (3). The remaining distance to entirely remove the particle equals $2r-D$. Because the particle covers this distance at the flow velocity, the total time needed to remove the particle is:

$$t_{er} = t_v + \frac{(2r - D)}{v_f} = \frac{m}{F} \times v_f + \frac{2r - D}{v_f} \tag{6}$$

Knowing the particle size and the time t_{er} needed to remove it, the erosion rate E ($m s^{-1}$) is given by:

$$E = \frac{2r}{t_{er}} \tag{7}$$

E is based on the balance between driving and resisting stresses. Fraccarollo and Capart (2002) and Medina et al. (2008) used similar approaches to determine erosion rates at the base of water surges and debris flows, without testing different flow rheologies. While some field studies suggest that incorporation may alter flow density during emplacement (Calder et al. 2000; Brand et al. 2014), we assume here that it remains constant during the bulking process. (Mc Dougall and Hungr 2005; Lê and Pitman 2009).

Rheology and nature of PDCs

Dense PDCs affect an erodible layer through basal shear stress, which slows down the flow, and through the normal stress of their weight. Because of the complex and not fully understood PDC behavior, different rheological laws, summarized in Kelfoun (2011), have been proposed to simulate these particular types of flows. Various degrees of PDC fluidization

Table 1 Main variables used in this study

Symbol	Variable	Value	Unit
g	Acceleration due to gravity ^a	9.81	m s^{-2}
r	Particle radius ^a	–	m
S_f	Contact area between a particule and the flow ^a	$4 r^2$	m^2
ρ_p	Particle density ^a	2500	kg m^{-3}
m	Particle mass ^a	–	kg
φ	Erodible bed repose angle ^a	–	degrees
C	Soil cohesion ^a	–	N
ρ_e	Flow density ^a	1300	kg m^{-3}
φ_{bed}	Flow basal friction angle ^a	–	degrees
T_0	Plastic constant retarding stress ^a	–	Pa
h_{erod}	Maximum erodible bed thickness ^b	–	m
α	Ground slope ^b	–	degrees
β	Flow surface slope angle	–	degrees
h	Flow thickness	–	m
v_f	Flow velocity	–	m s^{-1}
t	Time	–	s
T	Flow basal shear stress	–	Pa
T_F	Flow basal shear force	–	N
R	Resisting forces	–	N
W	Particle weight downstream component	–	N
F_b	Buoyancy force	–	N
F	Sum of external forces	–	N
t_v	Time to accelerate a particle at the velocity v_f	–	s
D	Distance traveled by a particle at a given time	–	m
D_v	Distance traveled by a particle at the time t_v	–	m
t_{er}	Total erosion time	–	s
E	Erosion rate	–	m s^{-1}

“Particle” refers to a particle from the erodible bed. Variable with no value implies variation in time or space during simulation

^a Input parameters

^b Input parameters recomputed for each time increment during dynamic simulations

can also be invoked (e.g., Sparks 1976; Roche et al. 2010, 2013). We investigate here two commonly used rheological laws, Coulomb and plastic behavior (Iverson and Denlinger 2001; Kelfoun et al. 2009; Charbonnier et al. 2013), coupled with different states of flow fluidization.

Coulomb rheology

The Coulomb law states that the shearing, T , exerted by the flow on its substrate depends on both the normal stress at the base of the flow and the friction angle φ_{bed} between the flow and its substrate. Values of φ_{bed} to numerically reproduce flow runout distances compatible with natural PDCs range between 10 and 15° (Patra et al. 2005; Kelfoun et al. 2009; Procter et al. 2010; Sulpizio et al. 2010; Kelfoun 2011; Charbonnier and Gertisser 2012).

The shear stress T exerted by a Coulomb flow on the erodible bed can be expressed as

$$T = \rho_e g h \cos \alpha \tan \varphi_{\text{bed}} \quad (8)$$

where g is the acceleration due to gravity (9.81 m s^{-1}), α is the slope angle, ρ_e is the density of the flow, h its thickness, and φ_{bed} its basal friction angle.

Plastic rheology

Kelfoun et al. (2009) and Charbonnier and Gertisser (2012) argued that a plastic rheology is appropriate for numerical modeling of PDCs (a statement that is debated in Kelfoun 2011). The plastic shear stress does not depend on flow thickness or velocity and is expressed as $T=T_0$. A possible explanation is that the plastic rheology captures, to a first order, the complex physics that reduces friction between particles, allowing PDCs to reach extended runouts. However, the constant retarding stress may locally induce an apparent basal friction angle, which is higher than the friction angle between particles at rest (see Eq. (8) and (9)) for flows thinner than

$$h < \frac{T}{\rho_e g \cos \alpha \tan \varphi_{\text{max}}} \quad (9)$$

where φ_{max} is the maximal internal friction angle between particles (which is the internal friction angle of particles at rest, about 30°, Yamashita and Miyamoto 1993). To avoid these conditions, we use a modified plastic law, called plastic- φ_{max} below, in which the plastic frictional stress cannot exceed the Coulomb stress of particles at rest.

The shear stress T exerted by a plastic- φ_{max} flow on the erodible bed is expressed as:

$$T = \min(T_0, \rho_e g h \cos \alpha \tan \varphi_{\text{max}}) \quad (10)$$

where T_0 is the constant plastic constant retarding stress.

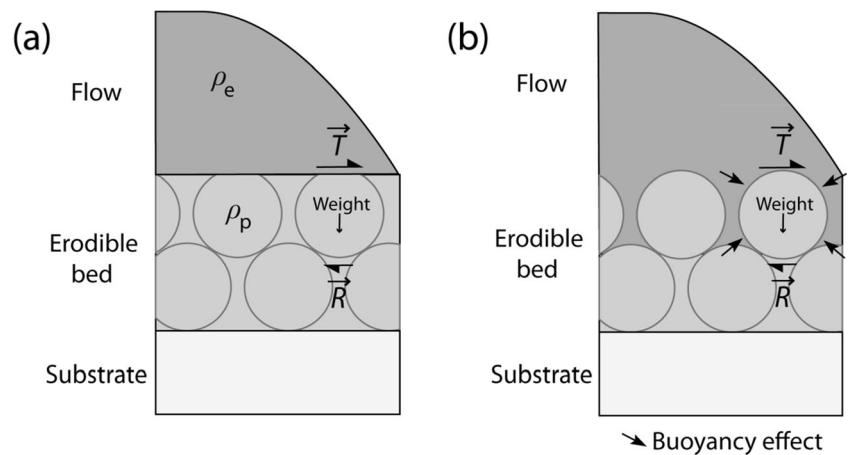
Non-fluidized flow model

As shown in Fig. 6a, a PDC is considered here as a sliding flow. In this case, the normal component of the flow weight is fully transmitted to the base of the erodible particles. The slope-parallel component of the weight W of the particle can be written as:

$$W = \frac{4}{3} \pi r^3 \rho_p g \sin \alpha \quad (11)$$

The total resistant forces, R , acting at the base of an erodible particle depend on the sum of the weight of the flow, and

Fig. 6 Cartoon depicting the flow regime assumptions used in this study. **a** Non-fluidized flow assumption: the flow is viewed as a block descending a slope and cannot fill the free space between removable particles. The flow acts on the particles only as a frictional body. **b** Fluid body assumption: the flow is able to percolate between the particles and generates both frictional and Archimedes-like forces (buoyancy effect)



of the weight, the friction angle φ and the bed cohesion C of the particle (Fig. 6 and Table 1):

$$R = \left(\rho_e h S_f + \frac{4}{3} \pi r^3 \rho_p \right) g \cos \alpha \tan \varphi + C \times S_f \quad (12)$$

Fluidized flow model

We state here that the PDC behaves as a fluid. The flow fills the holes between the bed particles, which can consequently be submitted to an upward buoyancy force, F_b , depending on the surface of contact (Fig. 6b). When the force affects only the upper hemisphere of the particle, no buoyancy effects occur, and the equations are those of the non-fluidized flow situation. When the whole particle surface is subjected to the flow fluid pressure, the buoyancy force is given by the expression:

$$F_b = \frac{4}{3} \pi r^3 \rho_e g \quad (13)$$

The slope-parallel component of the solid stress exerted at the base of a particle is thus expressed as:

$$W = \frac{4}{3} \pi r^3 g \left[\rho_p \sin \alpha - \rho_e \sin(\alpha - \beta) \right] \quad (14)$$

where β is the flow surface slope angle and the resisting force R given by:

$$R = \frac{4}{3} \pi r^3 g \left[\rho_p \cos \alpha - \rho_e \cos(\alpha - \beta) \right] \tan \varphi + C \times S_f \quad (15)$$

Varying the particle surface proportion impacted by the flow fluid pressure allows us to test various degree of fluidization.

Integration into VolcFlow code

The above erosion laws are first tested in stationary conditions. For the given flow rheology, fluidization state, and erodible bed characteristics, the erosion rate, E , is computed for a wide range of slope angles (from 0 to 90°). Slopes steeper than 40–50° are unrealistic at Tungurahua volcano but may be used to explore the erosion law behavior. In a second step, we run a numerical model of geophysical flows (VolcFlow code) to test these equations dynamically (i.e., in non-stationary conditions). VolcFlow simulates dynamic variations in thicknesses and velocity of dense isothermal volcanic flows based on the depth-averaged equations (Kelfoun and Druitt 2005). The code can also solve user-defined laws, such as those presented in this paper, and calculates their mass and momentum balance.

As our field study gives an image of the erosion pattern on the scale of the volcano, we fitted the pre-eruptive topography of the Juive Grande valley with an exponential expression, which captures the main characteristics of Tungurahua slopes and discards all small-scale topographic irregularities. The source mechanisms of the 2006 PDCs at Tungurahua are discussed in Kelfoun et al. (2009) and Hall et al. (2013): They resulted from repeated gravitational destabilizations of hot pyroclastic products (bombs, scoriae, and ash), which accumulated on the upper cone during the eruption. The initial flow velocities can therefore be set to zero. Input volumes in our simulations are in the order of 10^5 m^3 , which typically represents the volume of a single PDC unit in the Juive Grande valley for the 2006 Tungurahua paroxysm (Hall et al. 2013).

Results of numerical modeling

We present here the results obtained for stationary and dynamic conditions for both fluidized and non-fluidized flow assumptions, using a large range of values for Coulomb and

plastic rheologies (Table 2). In the following, when a parameter is not specified, the applied generic values (inferred from our field data and previous studies on Tungurahua 2006 PDCs; see Kelfoun et al. 2009) are: a 1-m-thick flow with a velocity of 10 m s^{-1} and a bulk density of $1,300 \text{ kg m}^{-3}$, a particle radius of 0.05 m, and density of $2,500 \text{ kg m}^{-3}$.

Fluidized body assumption

Under fluidized conditions, we found that erosion only occurs when the erodible particles are surrounded by the flow and affected by buoyancy. Figure 7 displays the variation of the erosion rate E (m s^{-1}) vs. the slope angle, when the particles are entirely surrounded by the flow, and for Coulomb (Fig. 7a) and plastic- φ_{max} (Fig. 7b) rheologies, respectively. Results show that the erosion rate is important ($>0.5 \text{ m s}^{-1}$) regardless of the slope angle and the rheological model (Fig. 7). E is also higher on gentle slopes than on steep ones. This can be explained by the vertical buoyancy stress relative to the slope angle: The buoyancy effect is maximal where the slope is close to horizontal. Other simulations using parameters in the range of those given in Table 2 yield an overall behavior similar to that displayed in Fig. 7. We find no combination of input parameters that reproduce the observed erosion pattern using the fluid flow assumption, even when different particle surface proportions in contact with the fluid flow are considered.

Non-fluidized flow assumption

Coulomb rheology Figure 8a shows the slope-dependent erosion rate, E , for six Coulomb basal friction angles (from 15 to 45°) under stationary conditions. To avoid any confusion, the erodible particle stability domain, as well as realistic Tungurahua slope angles, are highlighted. Figure 8a shows that the PDC's ability to incorporate particles from the erodible bed is associated with the basal friction angle of the flow. Importantly, the basal friction angle is a key parameter in the Coulomb rheology that controls the final runout distance. In theoretical stationary conditions, a 32° basal friction flow is able to erode material on slopes as

steep as 17° (Fig. 8a), but such a flow is unable to reach these gentle slopes because its high basal friction angle of 32° hampers propagation on slopes $<30^\circ$. Figure 8b presents three dynamic simulations performed with VolcFlow with three different Coulomb basal friction angles and shows the predicted final runout distance on Tungurahua's slope. Flows with runout distances consistent with that of the 2006 PDCs (i.e., with a 15° basal friction angle) are not able to dig into the erodible bed. Conversely, flows that reproduce our field-based erosion pattern in stationary conditions (basal friction angle of $30\text{--}32^\circ$ in Fig. 8a) are not able to dynamically reproduce them because the required basal friction angle of $30\text{--}32^\circ$ prevents the flow from reaching the foot of the volcano. Tests with different combinations of parameters (Table 2) fail to reproduce the 2006 PDC erosion pattern. Coulomb flow simulations tend to stabilize the erodible layer due to the flow weight component, which rapidly exceeds the flow shearing related to the basal friction angle, thus impeding particle entrainment. The basal friction angle of $\sim 15^\circ$ inherent to Coulomb rheology and required to reproduce the runout distances of the 2006 PDCs is too low to remove particles from the erodible bed and thus to reproduce the erosion pattern.

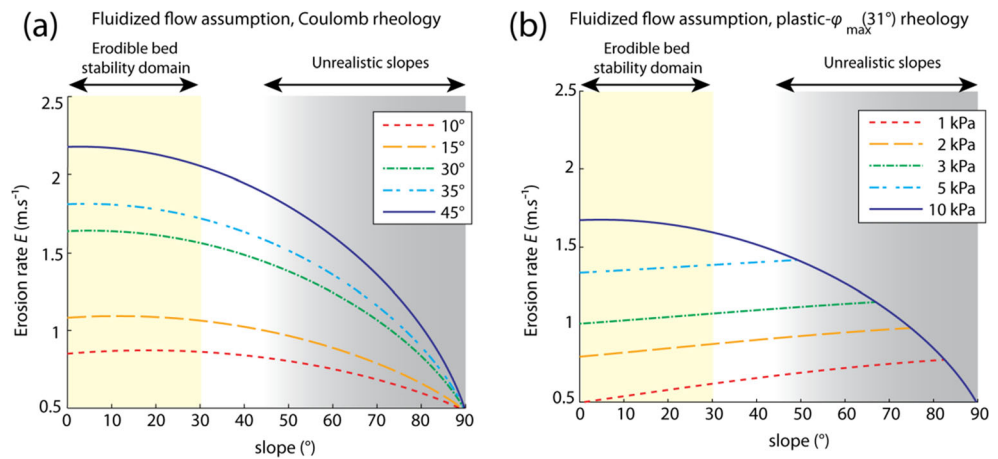
Plastic rheology Figure 9a shows the erosion rate, E , vs. the slope angle for a plastic- φ_{max} flow rheology ($T_0=5 \text{ kPa}$) of different thicknesses in stationary conditions. We tested φ_{max} in the range of $30\text{--}35^\circ$ and a value of 31° matches the erosion pattern best. The erosion rate curves of thick (1 to 5 m) flows include a break in slope (Fig. 9a) due to the threshold effect of the φ_{max} angle. This kink corresponds to the point where the apparent friction angle caused by the plastic stress reaches unrealistic values and is corrected by Eq. (10). Depending on the flow thickness, E is high on steep slopes and equals zero on slope angles lower than $\sim 25^\circ$, which is consistent with our field data. However, arrows on Fig. 9a show the lower theoretical slopes on which the modeled PDCs can flow. As with the Coulomb rheology, PDCs reproducing the erosion pattern (e.g., the 0.5 m-thick flow) are not able to reach the base of the volcano. In contrast, thick flows (e.g., 2 m thick) cannot entrain the erodible bed but can reach the runout distances measured at Tungurahua.

Table 2 Range of input parameters investigated in this work

Fluid. state	Rheology	Rheological parameters	h (m)	% aff. surf.
Fluidized	Coulomb	$\varphi_{\text{bed}}=10\text{--}45^\circ$ (10–45)	0.1–5 (1)	0–100 (100)
	Plastic- φ_{max}	$T=1\text{--}10 \text{ kPa}$ (1–10), $\varphi_{\text{max}}=30\text{--}35^\circ$ (31)	0.1–5 (1)	0–100 (100)
Non-fluidized	Coulomb	$\varphi_{\text{bed}}=10\text{--}45^\circ$ (10–45)	0.1–5 (1)	x
	Plastic- φ_{max}	$T=1\text{--}10 \text{ kPa}$ (5), $\varphi_{\text{max}}=30\text{--}35^\circ$ (31)	0.1–5 (0.1–5)	x

Results using the values in brackets are shown in Figs. 7, 8, and 9. See Table 1 for symbols' significance. "Fluidization state" refers to fluidization assumption (see text), and the "% stressed surface" is the percentage of particle surface area affected by the flow in the fluid assumption model. Other tested parameters are particle radius, r (0.01–1 m) and density, ρ_p ($1,500\text{--}3,000 \text{ kg m}^{-3}$), erodible bed thickness, h_{erod} (0–10 m), and erodible bed cohesion, C (1–20 kPa)

Fig. 7 Erosion rates, E , ($m s^{-1}$) vs. slope angle in stationary conditions for the fluidized flow assumption. **a** Coulomb rheology with different values of basal friction angle. **b** Plastic- φ_{max} rheology with different values of retarding stress and a maximum basal friction angle φ_{max} of 31° . Other parameters are generic values presented in the text, see also Table 2



Dynamically, results are clearly different. Figure 9b shows numerical results obtained with VolcFlow for the realistic slope angles of Tungurahua volcano and with the same variables used in Fig. 9a (plastic- φ_{max} rheology, $T_0=5$ kPa and $\varphi_{max}=31^\circ$). Both erosion and runouts are in good agreement with field-based inferences: Erosion is localized on slope angles steeper than $\sim 25^\circ$ ($>3,500$ m asl), and PDC runout distances are consistent with those determined in the field. We noted during our simulations that dynamic variations of flow thickness play a major role in the shear stress-related erosion: Where and when the flow is thick, the shear stress is low relative to the normal components of the weight that stabilize the particles. Erosion does not occur, and the flow can move on gentle slopes (Fig. 9a). The driving stresses accelerate such a thick flow, which becomes thinner, causing an increase in the shear stress relative to the weight components. As a consequence, the erosive flow capacity is enhanced

and erosion begins. At the same time, the velocity decreases (due to an increase in the resistive stress/driving stress ratio), causing the flow to thicken again, impeding erosion and promoting further mobility, even on gentle slopes. During emplacement, the flow thus dynamically oscillates between a low velocity erosive phase and a non-erosive phase, consistent with the main characteristics of the 2006 PDCs erosion pattern.

Discussion

Localization of erosion and significance of componentry

Discussing the details of the componentry data is beyond the scope of this work, in which we concentrate on deciphering the main processes that may account for the large amount of

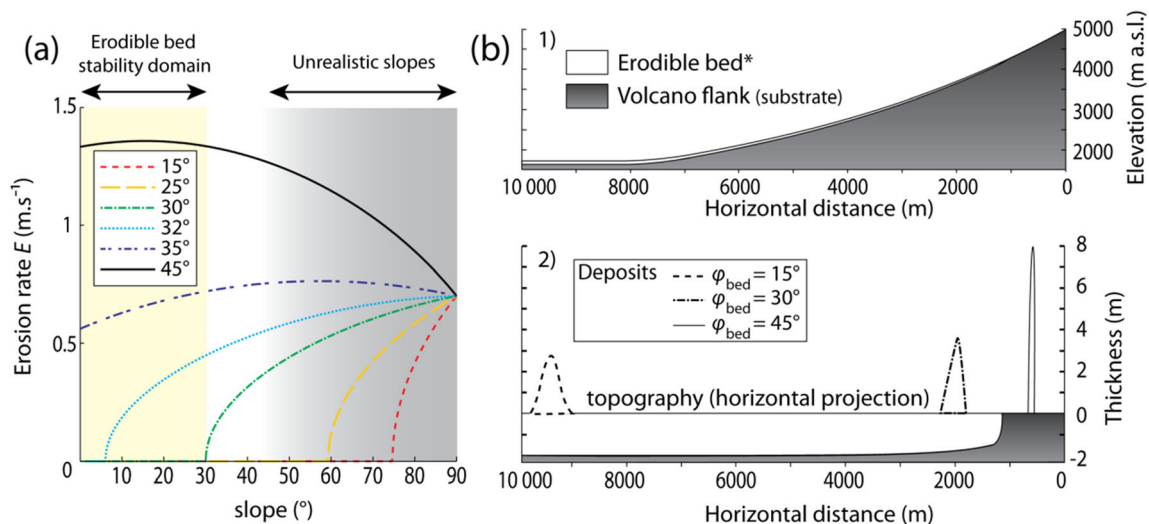


Fig. 8 **a** Erosion rates, E , ($m s^{-1}$) vs. slope angle for a non-fluidized flow assumption with a Coulomb rheology and for different basal friction angles φ_{bed} in stationary conditions. Other parameters are generic values presented in the text, see also Table 2. **b** 1) Tungurahua's profile (in dark gray) and erodible bed (white layer, vertical exaggeration of five for

legibility) used for the non-stationary simulations; 2) horizontal projection of final VolcFlow dynamic simulation results conducted with a Coulomb rheology and different basal friction angles φ_{bed} of 15, 30, and 45° . Dashed lines represent deposit contours and illustrate the runout distance of each flow. The erodible bed is not removed by the PDCs

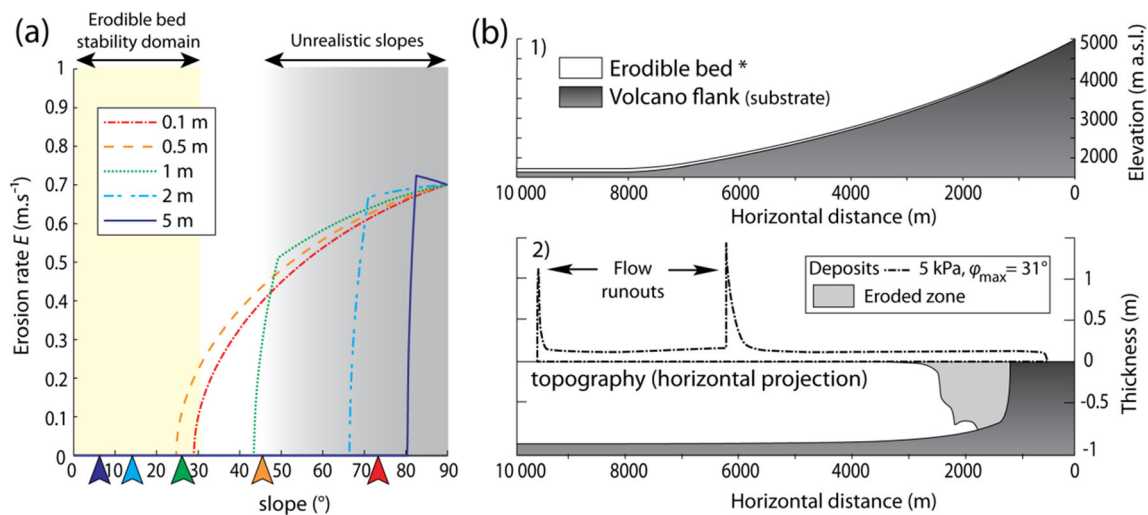


Fig. 9 **a** Erosion rate vs. slope angle for the non-fluidized assumption with a plastic- φ_{\max} rheology ($T=5$ kPa; $\varphi_{\max}=31^\circ$) in stationary conditions. The curves correlate to different flow thickness, and *colored arrows* on the slope axis show the slope angle at which each flow stops. Other parameters are generic values presented in the text (see also Table 2). The domain of erodible bed stability and the field of unrealistic slopes are

shown. **b** 1 Tungurahua's profile and erodible bed used for the simulations; 2 horizontal projection of final VolFlow dynamic simulation results obtained with a plastic- φ_{\max} rheology ($T=5$ kPa; $\varphi_{\max}=31^\circ$). Deposit contours are represented as *dashed lines* and illustrate flow runout. The remobilized fraction of the erodible layer (in *pale gray*) is only localized on steep slopes of the upper cone, above 3,500 m asl

non-juvenile material in the deposits. An important issue that we address in a forthcoming paper is the impact of the digital background on volume and juvenile/non juvenile mass ratios. Estimations based on available componentry data in the matrix fraction (Hall et al. 2013; and unpublished data) suggest that our assumption about the digital background componentry assemblage does not significantly alter our estimates of juvenile/non-juvenile ratios.

An important result of this work is that, although sampling was carried out at only eight sites (five locations) along the Juive Grande valley, little variation in the juvenile/non-juvenile ratio is observed. The highest sampling sites display a juvenile content of 40–50 wt%, while the lowermost samples near the road to Baños yield 50–60 wt%. We infer that erosion and incorporation essentially took place high on the steepest slopes of the volcano, in the upper morphological domain, resulting in 40–50 wt% incorporation at about 3,500 m asl. In contrast, later erosion and incorporation in the intermediate and lower morphological domains likely account for only a few weight percentages, i.e., one order of magnitude less than that on the upper cone, and this can be explained by topographic irregularities along PDC paths (e.g., small-scale breaks in slope and cliffs and narrow gullies) as also noted at Arenal by Cole et al. (2005). This finding indicates that little or no erosion took place during emplacement in the Juive valley below $\sim 3,500$ m asl (i.e., on slope angles $<25^\circ$), while deposition began on slope angles in the range of $25\text{--}30^\circ$ and the eroded material accounts for half of the total mass of PDC deposits. Similar erosion patterns are documented at many volcanoes worldwide: 35–46 wt% of non-juvenile components were found in the -4 to 4 ϕ range of

scoria flow deposits from the 1991 eruption of Volcán de Colima, Mexico (Saucedo et al. 2004), while erosion mainly occurred on near-to-vent slope angles $>20\text{--}30^\circ$ at Arenal, Costa Rica (Cole et al. 2005), Ngauruhoe, New-Zealand (Lube et al. 2007) and Merapi, where non-juvenile material represents up to 20 wt% of the 2006 block and ash flow deposits (Charbonnier and Gertisser 2011). In other geological contexts, entrainment of rock and debris occurs on slope angles $>20\text{--}25^\circ$ and is associated with an increase in >50 wt% in wet rock and snow avalanches (Hung and Evans 2004; Hung et al. 2005; Sovilla et al. 2006). These erosion patterns are consistent with analogue models of granular flows, which show that steeper slope angles alter the erosion pattern and enhance the erosion rate (Mangeney et al. 2010; Farin et al. 2013; and references therein).

Striated slide-like scoured paths exposing massive lavas of the upper cone of Tungurahua were observed soon after the August 17th eruption and recall those documented at other volcanoes (Lascar, Sparks et al. 1997; Ngauruhoe, Lube et al. 2007; Merapi, Cronin et al. 2013). The high mechanical resistance of these lavas limits the thickness of the erodible bed until formation of chute-like channels, in which the erodible material is no longer available. This observation highlights the critical role of the erodible bed's nature and thickness on erosion processes. At a given PDC volume flowing downslope, the amount of the available erodible supply (i.e., the erodible bed thickness, Sparks et al. 1997; Hung et al. 2005) is one of the key parameters controlling the proportion of non-juvenile component incorporated into the PDC and thus the resulting increase in volume and mass. The ability of a flow to erode its substrate depends on parameters linked

to the eruptive process (initial volume of juvenile products and the PDC feeding mechanism) and to non-eruptive parameters (slope angle, erodible bed nature, and thickness).

Erosion law

In our models, the displacement of particles is controlled by the difference between the shear stresses of the flow that destabilizes them, and the resisting stress of the substrate. The flow basal shear stress required for long runout distances should be low (i.e., φ_{bed} , $\sim 10\text{--}15^\circ$ for Coulomb rheology or T_0 , $\sim 3\text{--}5$ kPa for plastic rheology). In those conditions, only fluidized flows can be erosive, but their erosion patterns conflict with observations made at Tungurahua. In the case of non-fluidized flows, the counter-intuitive proposition, as illustrated by the stationary condition tests, is that the flow basal shear stress should be high (whatever the rheology is) in order to initiate entrainment of the erodible bed, which conflicts with long runout flows observed in nature. When incorporated into a numerical model that simulates dynamic flow emplacement, our equations show that PDCs can both reach long runout distances and be erosive due to variations in the normal stress/basal shear stress ratio in time and space. Where and when the basal stress is low, the flow can move, even on gentle slopes. Where and when the basal stress is high relative to the normal stress, the flow is able to dig into the erodible bed. For a Coulomb rheology, this ratio is constant and fixed by the basal friction angle, which hampers reproducing the 2006 PDC erosion pattern. In the plastic- φ_{max} rheology, the basal shear stress is constant, implying that the normal stress/basal shear stress ratio (which determine the flow velocity) depends on the flow thickness.

In the model, these thickness variations are linked to two different processes. During emplacement, the PDC propagates dynamically in pulses (Schwarzkopf et al. 2005; Sulpizio and Dellino 2008; Kelfoun et al. 2009; Charbonnier and Gertisser 2012), which implies thickness variations in time and space. Thick and non-erosive parts of the flow accelerate. As a consequence, the flow thins and the normal vs. shear stress ratio decreases, thus causing flow deceleration and bed erosion. This erosional mechanism was also observed by Mangeney et al. (2010) and Farin et al. (2013) in laboratory experiments. In addition, flow shape also controls the erosion process during emplacement. A moving flow comprises a thick body with a lobate and thicker head that rapidly thins at the front. By itself, this thin frontal part would not be able to move, but it is pushed downwards to gentle slopes by thicker parts of the flow. Merging these two parts of the flow triggers entrainment and incorporation and may explain erosion patterns and runouts of the 2006 PDCs. Nevertheless, there are several caveats when using this simple model, and it is worth noting that additional mechanisms may explain the shear stress fluctuation in natural flows. For example, different

degrees of fluidization of a moving flow can cause alternating increase and decrease in the normal stress/basal shear stress ratios (Sulpizio and Dellino 2008). The transport of blocks that temporarily slide and tumble within a low-shearing flow may also explain a part of the erosion pattern (Grunewald et al. 2000).

The published literature lacks estimates of field-derived PDC-induced erosion rates. Nevertheless, Iverson (2012) modeled wet substrate entrainment by debris flows and determined erosion rates of between 0.05 m s^{-1} (high degree of flow liquefaction) and 0.2 m s^{-1} (low degree) on a slope of 31° , a flow thickness of 0.2 m, and a velocity of 12 m s^{-1} . This is close to the erosion rate of 0.21 m s^{-1} computed in this study with the same parameters (slope of 31° , flow thickness of 0.2 m, and velocity of 12 m s^{-1}), which is consistent with large-scale debris flow experiments and in situ measurements (Mc Coy et al. 2012; Iverson 2012 and references therein). The erosion rates estimated here are moreover close to those determined in the laboratory experiments of Mangeney et al. (2010) rescaled from experimental velocity and flow thickness.

Conclusions

Grain size and componentry analysis combined with 2D–3D stereological corrections performed on digital image samples of PDC deposits from the August 16th, 2006 eruption of Tungurahua volcano have allowed us to determine juvenile vs. non-juvenile mass fractions in the deposits at selected locations in the Juive Grande valley. Our results reveal that the August 2006 PDCs incorporated about 40–50 wt% of accessory and accidental material, principally in the upper cone domain where slope angles are $>25^\circ$.

These componentry results were used to evaluate the accuracy of a shear stress-related equation of PDC-induced erosion. Because PDC rheology is still not fully understood, we investigated both Coulomb and plastic rheologies, which are commonly used for numerical modeling of PDC emplacement, and made assumptions on the degree of fluidization. Our erosion equation was tested under stationary and non-stationary conditions to infer flow behavior (using VolcFlow code). The comparison of numerical and componentry results shows that the first-order parameters of PDC-induced erosion during the 2006 eruption of Tungurahua can be reproduced using a plastic- φ_{max} rheology.

Our model reproduces the PDC erosion pattern solely to the first order but offers new insights into PDC dynamics with implications for hazard assessment purposes. Comparing a plastic- φ_{max} PDC flowing over a non-erodible substrate and on a 1-m-thick erodible bed allows the influence of erosion and bulking processes on dense PDC mobility to be quantified. A

major outcome is that entrainment tends to decelerate the flow, while the incorporation processes increase flow thickness, which cancels the slowdown effect of entrainment and enhances flow runout distances. In the case of a small-volume PDC ($\sim 3 \times 10^5 \text{ m}^3$) with a bulking of 40 vol.% (i.e., corresponding to a 1-m-thick erodible bed), the runout distance is increased by up to 4–20 %, depending on slope angle to the base of the edifice (0–10°). This finding extends those obtained by analogue models on a constant slope using a Coulomb rheology (Mangeney et al. 2010; Farin et al. 2013).

Our exploratory numerical model suggests that bulking on steep slopes of andesitic volcanoes increases the volume, the velocity, and the runout distance of PDCs. On slopes steeper than $\sim 25^\circ$, the flows may remove all the particles down to the substrate. Therefore, the presence of large amounts of tephra and blocks on such slopes prior to PDC emplacement may enhance their destructive effect.

Acknowledgments This work is part of a PhD project by JB and has been completed in the context of a French-Ecuadorian cooperation program. We thank the Laboratoire Mixte International of IRD “Séismes et Volcans dans les Andes du Nord” for financial support. We thank V. Manville for editorial handling as well as S. Charbonnier, R Sulpizio, and an anonymous reviewer for constructive criticism on the manuscript. This is Laboratory of Excellence ClerVolc contribution number 134.

References

- Arellano SR, Hall M, Samaniego P, Le Pennec JL, Ruiz A, Molina I, Yepes H (2008) Degassing patterns of Tungurahua volcano (Ecuador) during the 1999–2006 eruptive period, inferred from remote spectroscopic measurements of SO₂ emissions. *J Volcanol Geotherm Res* 176(1):151–162
- Auker MR, Sparks RSJ, Siebert L, Crowther HS, Ewert J (2013) A statistical analysis of the global historical volcanic fatalities record. *J Appl Volcanol* 2(1):2
- Bouchut F, Fernández-Nieto ED, Mangeney A, Lagrée PY (2008) On new erosion models of Savage–Hutter type for avalanches. *Acta Mech* 199(1–4):181–208
- Boudon G, Camus G, Gourgaud A, Lajoie J (1993) The 1984 nuée-ardente deposits of Merapi volcano, Central Java, Indonesia: stratigraphy, textural characteristics, and transport mechanisms. *Bull Volcanol* 55(5):327–342
- Brand BD, Mackaman-Lofland C, Pollock NM, Bendaña S, Dawson B, Wichgers P (2014) Dynamics of pyroclastic density currents: conditions that promote substrate erosion and self-channelization - Mount St Helens, Washington (USA). *J Volcanol Geotherm Res* 276:189–214
- Branney MJ, Kokelaar BP (2002) Pyroclastic density currents and the sedimentation of ignimbrites. *Geol Soc Mem No* 27:143
- Buesch DC (1992) Incorporation and redistribution of locally derived lithic fragments within a pyroclastic flow. *Geol Soc Am Bull* 104(9):1193–1207
- Calder ES, Sparks RSJ, Gardeweg MC (2000) Erosion, transport and segregation of pumice and lithic clasts in pyroclastic flows inferred from ignimbrite at Lascar Volcano, Chile. *J Volcanol Geotherm Res* 104(1–4):201–235
- Cao Z, Pender G, Wallis S, Carling P (2004) Computational dam-break hydraulics over erodible sediment bed. *J Hydraul Eng* 130(7):689–703
- Carn SA, Krueger AJ, Arellano S, Krotkov NA, Yang K (2008) Daily monitoring of Ecuadorian volcanic degassing from space. *J Volcanol Geotherm Res* 176(1):141–150
- Cas RA, Wright JV (1987) Volcanic successions, modern and ancient: a geological approach to processes, products, and successions. Allen & Unwin, London, p 528
- Charbonnier SJ, Gertisser R (2011) Deposit architecture and dynamics of the 2006 block-and-ash flows of Merapi Volcano, Java, Indonesia. *Sedimentology* 58(6):1573–1612
- Charbonnier SJ, Gertisser R (2012) Evaluation of geophysical mass flow models using the 2006 block-and-ash flows of Merapi Volcano, Java, Indonesia: towards a short-term hazard assessment tool. *J Volcanol Geotherm Res* 231–232:87–108
- Charbonnier SJ, Germa A, Connor CB, Gertisser R, Preece K, Komorowski JC, Lavigne F, Dixon T, Connor L (2013) Evaluation of the impact of the 2010 pyroclastic density currents at Merapi volcano from high-resolution satellite imagery, field investigations and numerical simulations. *J Volcanol Geotherm Res* 261:295–315
- Cole PD, Fernandez E, Duarte E, Duncan AM (2005) Explosive activity and generation mechanisms of pyroclastic flows at Arenal volcano, Costa Rica between 1987 and 2001. *Bull Volcanol* 67(8):695–716
- Cronin SJ, Lube G, Dayudi DS, Sumarti S, Subrandiyo S, Surono (2013) Insights into the October–November 2010 Gunung Merapi eruption (Central Java, Indonesia) from the stratigraphy, volume and characteristics of its pyroclastic deposits. *J Volcanol Geotherm Res* 261:244–259
- Crosta GB, Imposimato S, Roddeman D (2009) Numerical modelling of entrainment/deposition in rock and debris-avalanches. *Eng Geol* 109(1–2):135–145
- Dellino P, Büttner R, Dioguardi F, Doronzo DM, La Volpe L, Mele D, Sonder I, Sulpizio R, Zimanowski B (2010) Experimental evidence links volcanic particle characteristics to pyroclastic flow hazard. *Earth Planet Sci Lett* 295(1–2):314–320
- Douillet G, Tsang-Hin-Sun È, Kueppers U, Letort J, Pacheco D, Goldstein F, Aulock F, Lavallée Y, Hanson J, Bustillos J, Robin C, Ramón P, Hall M, Dingwell D (2013) Sedimentology and geomorphology of the deposits from the August 2006 pyroclastic density currents at Tungurahua volcano, Ecuador. *Bull Volcanol* 75(11):1–21
- Druitt TH (1998) Pyroclastic density currents. *Geol Soc Lond, Spec Publ* 145(1):145–182
- Egashira S, Honda N, Itoh T (2001) Experimental study on the entrainment of bed material into debris flow. *Phys Chem Earth C Solar Terr Planet Sci* 26(9):645–650
- Eychenne J, Le Pennec J-L (2012) Sigmoidal particle density distribution in a subplinian scoria fall deposit. *Bull Volcanol* 74(10):2243–2249
- Eychenne J, Le Pennec J-L, Troncoso L, Gouhier M, Nedelec J-M (2012) Causes and consequences of bimodal grain-size distribution of tephra fall deposited during the August 2006 Tungurahua eruption (Ecuador). *Bull Volcanol* 74(1):187–205
- Eychenne J, Le Pennec J-L, Ramón P, Yepes H (2013) Dynamics of explosive paroxysms at open-vent andesitic systems: high-resolution mass distribution analyses of the 2006 Tungurahua fall deposit (Ecuador). *Earth Planet Sci Lett* 361:343–355
- Farin M, Mangeney A, Roche O (2013) Fundamental changes of granular flow dynamics, deposition and erosion processes at high slope angles: insights from laboratory experiments. *J Geophys Res Earth Surf* 2013JF002750
- Fee D, Garces M, Steffke A (2010) Infrasound from Tungurahua Volcano 2006–2008: Strombolian to Plinian eruptive activity. *J Volcanol Geotherm Res* 193(1–2):67–81
- Fracarollo L, Capart H (2002) Riemann wave description of erosional dam-break flows. *J Fluid Mech* 461:183–228
- Grunewald U, Sparks RSJ, Keams S, Komorowski JC (2000) Friction marks on blocks from pyroclastic flows at the Soufriere Hills

- volcano, Montserrat: implications for flow mechanisms. *Geology* 28(9):827–830
- Gurioli L, Cioni R, Sbrana A, Zanella E (2002) Transport and deposition of pyroclastic density currents over an inhabited area: the deposits of the AD 79 eruption of Vesuvius at Herculaneum, Italy. *Sedimentology* 49(5):929–953
- Hall ML, Robin C, Bernardo B, Mothes P, Monzier M (1999) Tungurahua Volcano, Ecuador: structure, eruptive history and hazards. *J Volcanol Geotherm Res* 91:1–21
- Hall ML, Steele AL, Mothes PA, Ruiz MC (2013) Pyroclastic density currents (PDC) of the 16–17 August 2006 eruptions of Tungurahua volcano, Ecuador: geophysical registry and characteristics. *J Volcanol Geotherm Res* 265:78–93
- Hungr O, Evans SG (2004) Entrainment of debris in rock avalanches: an analysis of a long run-out mechanism. *Geol Soc Am Bull* 116(9–10):1240–1252
- Hungr O, McDougall S, Bovis M (2005) Entrainment of material by debris flows. In: Jakob M, Hungr O, Jakob DM (eds) *Debris-flow hazards and related phenomena*. Springer, Berlin Heidelberg, pp 135–158
- Iverson RM (2012) Elementary theory of bed-sediment entrainment by debris flows and avalanches. *J Geophys Res* 117(F3)
- Iverson RM, Denlinger RP (2001) Flow of variably fluidized granular masses across three-dimensional terrain: 1. Coulomb mixture theory. *J Geophys Res Solid Earth* 106(B1):537–552
- Iverson RM, Reid ME, Logan M, LaHusen RG, Godt JW, Griswold JP (2011) Positive feedback and momentum growth during debris-flow entrainment of wet bed sediment. *Nat Geosci* 4(2): 116–121
- Jessop DE, Kelfoun K, Labazuy P, Mangeney A, Roche O, Tillier JL, Trouillet M, Thibault G (2012) LiDAR derived morphology of the 1993 Lascar pyroclastic flow deposits, and implication for flow dynamics and rheology. *J Volcanol Geotherm Res* 245–246:81–97
- Kelfoun K (2011) Suitability of simple rheological laws for the numerical simulation of dense pyroclastic flows and long-runout volcanic avalanches. *J Geophys Res* 116(B8)
- Kelfoun K, Druitt TH (2005) Numerical modeling of the emplacement of Socoma rock avalanche, Chile. *J Geophys Res Solid Earth* 110(B12), B12202
- Kelfoun K, Samaniego P, Palacios P, Barba D (2009) Testing the suitability of frictional behaviour for pyroclastic flow simulation by comparison with a well-constrained eruption at Tungurahua volcano (Ecuador). *Bull Volcanol* 71(9):1057–1075
- Launeau P, Robin P-YF (1996) Fabric analysis using the intercept method. *Tectonophysics* 267(1):91–119
- Le Pennec J-L, Jaya D, Samaniego P, Ramón P, Moreno Yáñez S, Egred J, van der Plicht J (2008) The AD 1300–1700 eruptive periods at Tungurahua volcano, Ecuador, revealed by historical narratives, stratigraphy and radiocarbon dating. *J Volcanol Geotherm Res* 176(1):70–81
- Le Pennec J-L, Ruiz GA, Ramón P, Palacios E, Mothes P, Yepes H (2012) Impact of tephra falls on Andean communities: the influences of eruption size and weather conditions during the 1999–2001 activity of Tungurahua volcano, Ecuador. *J Volcanol Geotherm Res* 217–218:91–103
- Le Pennec J-L, de Saulieu G, Samaniego P, Jaya D, Gailler L (2013) A devastating Plinian eruption at Tungurahua Volcano reveals formative occupation at ~1100 cal BC in Central Ecuador. *Radiocarbon* 55(3–4)
- Lê L, Pitman EB (2009) A model for granular flows over an erodible surface. *Siam J Appl Math* 70(5):1407–1427
- Lube G, Cronin SJ, Platz T, Freundt A, Procter JN, Henderson C, Sheridan MF (2007) Flow and deposition of pyroclastic granular flows: a type example from the 1975 Ngauruhoe eruption, New Zealand. *J Volcanol Geotherm Res* 161(3):165–186
- Mangeney A, Tsimring LS, Volfson D, Aranson IS, Bouchut F (2007) Avalanche mobility induced by the presence of an erodible bed and associated entrainment. *Geophys Res Lett* 34(22), L22401
- Mangeney A, Roche O, Hungr O, Mangold N, Faccanoni G, Lucas A (2010) Erosion and mobility in granular collapse over sloping beds. *J Geophys Res* 115(F3), F03040
- Mc Coy SW, Kean JW, Coe JA, Tucker GE, Staley DM, Wasklewicz TA (2012) Sediment entrainment by debris flows: in situ measurements from the headwaters of a steep catchment. *J Geophys Res* 117(No. F3)
- Mc Dougall S, Hungr O (2005) Dynamic modelling of entrainment in rapid landslides. *Can Geotech J* 42(5):1437–1448
- Medina V, Hürlimann M, Bateman A (2008) Application of FLATModel, a 2D finite volume code, to debris flows in the northeastern part of the Iberian Peninsula. *Landslides* 5(1):127–142
- Naaim M, Faug T, Naaim-Bouvet F (2003) Dry granular flow modelling including erosion and deposition. *Surv Geophys* 24:569–585
- Patra AK, Bauer AC, Nichita CC, Pitman EB, Sheridan MF, Bursik M, Rupp B, Webber A, Stinton AJ, Namikawa LM, Renschler CS (2005) Parallel adaptive numerical simulation of dry avalanches over natural terrain. *J Volcanol Geotherm Res* 139(1–2):1–21
- Pirulli M, Pastor M (2012) Numerical study on the entrainment of bed material into rapid landslides. *Geotechnique* 62(11):959–972
- Pitman E, Nichita C, Patra A, Bauer A, Bursik M, Weber A (2003) A model of granular flows over an erodible surface. *Discret Contin Dyn Syst B* 3(4):589–600
- Procter JN, Cronin SJ, Platz T, Patra A, Dalbey K, Sheridan M, Neall V (2010) Mapping block-and-ash flow hazards based on Titan 2D simulations: a case study from Mt. Taranaki, NZ. *Nat Hazards* 53(3):483–501
- Quan Luna B, Remaître A, van Asch TWJ, Malet JP, van Westen CJ (2012) Analysis of debris flow behavior with a one dimensional run-out model incorporating entrainment. *Eng Geol* 128:63–75
- Roche O, Montserrat S, Niño Y, Tamburrino A (2010) Pore fluid pressure and internal kinematics of gravitational laboratory air-particle flows: insights into the emplacement dynamics of pyroclastic flows. *J Geophys Res Solid Earth* 115(B9), B09206
- Roche O, Niño Y, Mangeney A, Brand B, Pollock N, Valentine GA (2013) Dynamic pore-pressure variations induce substrate erosion by pyroclastic flows. *Geology* 41(10):1107–1110
- Sahagian DL, Proussevitch AA (1998) 3D particle size distributions from 2D observations: stereology for natural applications. *J Volcanol Geotherm Res* 84:173–196
- Samaniego P, Le Pennec J-L, Robin C, Hidalgo S (2011) Petrological analysis of the pre-eruptive magmatic process prior to the 2006 explosive eruptions at Tungurahua volcano (Ecuador). *J Volcanol Geotherm Res* 199(1–2):69–84
- Sarocchi D, Sulpizio R, Macías JL, Saucedo R (2011) The 17 July 1999 block-and-ash flow (BAF) at Colima Volcano: new insights on volcanic granular flows from textural analysis. *J Volcanol Geotherm Res* 204(1–4):40–56
- Saucedo R, Macías JL, Bursik MI, Mora JC, Gavilanes JC, Cortes A (2002) Emplacement of pyroclastic flows during the 1998–1999 eruption of Volcán de Colima, México. *J Volcanol Geotherm Res* 117(1–2):129–153
- Saucedo R, Macías J, Bursik M (2004) Pyroclastic flow deposits of the 1991 eruption of Volcán de Colima, Mexico. *Bull Volcanol* 66(4): 291–306
- Schwarzkopf LM, Schmincke H-U, Cronin SJ (2005) A conceptual model for block-and-ash flow basal avalanche transport and deposition, based on deposit architecture of 1998 and 1994 Merapi flows. *J Volcanol Geotherm Res* 139(1–2):117–134
- Shea T, Houghton BF, Gurioli L, Cashman KV, Hammer JE, Hobden BJ (2010) Textural studies of vesicles in volcanic rocks: an integrated methodology. *J Volcanol Geotherm Res* 190:271–289

- Sovilla B, Burlando P, Bartelt P (2006) Field experiments and numerical modeling of mass entrainment in snow avalanches. *Journal of Geophysical Research: Earth Surface* 111(F3)
- Sparks RSJ (1976) Grain size variations in ignimbrites and implications for the transport of pyroclastic flows. *Sedimentology* 23(2):147–188
- Sparks RSJ, Wilson L, Hulme G (1978) Theoretical modeling of the generation, movement, and emplacement of pyroclastic flows by column collapse. *J Geophys Res Solid Earth* 83(B4):1727–1739
- Sparks RSJ, Gardeweg MC, Calder ES, Matthews SJ (1997) Erosion by pyroclastic flows on Lascar Volcano, Chile. *Bull Volcanol* 58:557–565
- Steffke AM, Fee D, Garces M, Harris A (2010) Eruption chronologies, plume heights and eruption styles at Tungurahua Volcano: integrating remote sensing techniques and infrasound. *J Volcanol Geotherm Res* 193(3–4):143–160
- Sulpizio R, Dellino P (2008) Chapter 2: Sedimentology, depositional mechanisms and pulsating behaviour of pyroclastic density currents. In: Gottsmann J, Marti J (eds) *Developments in volcanology*. Elsevier, pp 57–96
- Sulpizio R, Capra L, Sarocchi D, Saucedo R, Gavilanes-Ruiz JC, Varley NR (2010) Predicting the block-and-ash flow inundation areas at Volcán de Colima (Colima, Mexico) based on the present day (February 2010) status. *J Volcanol Geotherm Res* 193(1–2):49–66
- Tanguy JC, Ribière C, Scarth A, Tjetjep WS (1998) Victims from volcanic eruptions: a revised database. *Bull Volcanol* 60(2):137–144
- Yamashita S, Miyamoto K (1993) Model of pyroclastic flow and its numerical solution. *IAHS Publication*:67–67